Home   Search   Collections   Journals   About   Contact us   My IOPscience

A Bayesian approach for damage localization in plate-like structures using Lamb waves

A Bayesian approach for damage localization in plate-like structures using Lamb waves

Gang Yan

State Key Laboratory of Mechanics and Control of Mechanical Structures, Nanjing University of Aeronautics and Astronautics, Nanjing 210016, People's Republic of China

E-mail: yangang@nuaa.edu.cn

Abstract

This paper presents an investigation of the applicability of a Bayesian system identification theory for localizing damage in plate-like structures, while considering the uncertainties from modeling and measurement. Diagnostic Lamb waves are excited and received by a piezoelectric sensor network before and after damage to obtain scattered waves that contain characteristic information about the damage. After the time-of-flight (ToF) of the scattered waves in each actuator–sensor path is measured by a continuous wavelet transform (CWT), a Bayesian approach is developed to identify the damage location and wave velocity. By combining the prior information and the measured ToF data, Bayes' theorem is used to update the probability distributions of the parameters about the damage location and wave velocity. In particular, a Markov chain Monte Carlo (MCMC) method is employed for sampling the posterior distributions of the unknown parameters. A numerical study for an aluminum plate and experimental studies for a stiffened aluminum panel and a composite laminate are conducted to validate the proposed Bayesian damage localization approach.

(Some figures may appear in colour only in the online journal)

1. Introduction

Over the past twenty years, structural health monitoring (SHM) technology has gained significant attention in research and engineering communities. The increasing emphasis on the integrity of critical structures such as aircraft urges the needs to monitor the structures *in situ* and real-time to detect damage at an early stage to prevent catastrophic failure [1, 2]. Since the Lamb wave-based technique can detect small areas of local damage in plate-like structures, it is considered as a promising candidate in the application of future online SHM systems. A wide range of theoretical, numerical and experimental studies have been performed to assess the effectiveness and applicability of damage detection and identification using Lamb waves [3, 4].

Usually in the Lamb wave-based technique, piezoelectric transducers are embedded in or surface mounted on the structure both as actuators and sensors. When a diagnostic Lamb wave excited by the actuator encounters the damage, part of the wave will be scattered. Compared with the wave signals in the undamaged state (baseline signals), the scattered waves received by the sensors can be obtained simply by subtraction of the damaged and undamaged wave signals in each actuator–sensor path. The scattered waves contain characteristic information about the damage, and intuitively, the time-of-flight (ToF) of the scattered waves is related to the damage location. Thus, in the Lamb wave-based technique, using the ToF of the scattered waves to localize damage is a straightforward method [5–10]. For instance, Raghavan and Cesnik [5] used three collocated actuator/sensor pairs working on pulse-echo mode to localize damage; three circles of radii equal to the radial locations which are obtained by the product of the ToF of the damage-reflected waves and pre-calculated wave velocities intersect at the location of damage. For the sensor network working on pitch-catch mode, Kehlenbach *et al* [6] and Tua *et al* [7] employed a geometric approach with each pair of transducers as the foci of an ellipse of possible damage location. Figure 1(a) shows an illustration of this ellipse damage localization method in the case of using three actuator/sensor pairs. The point at
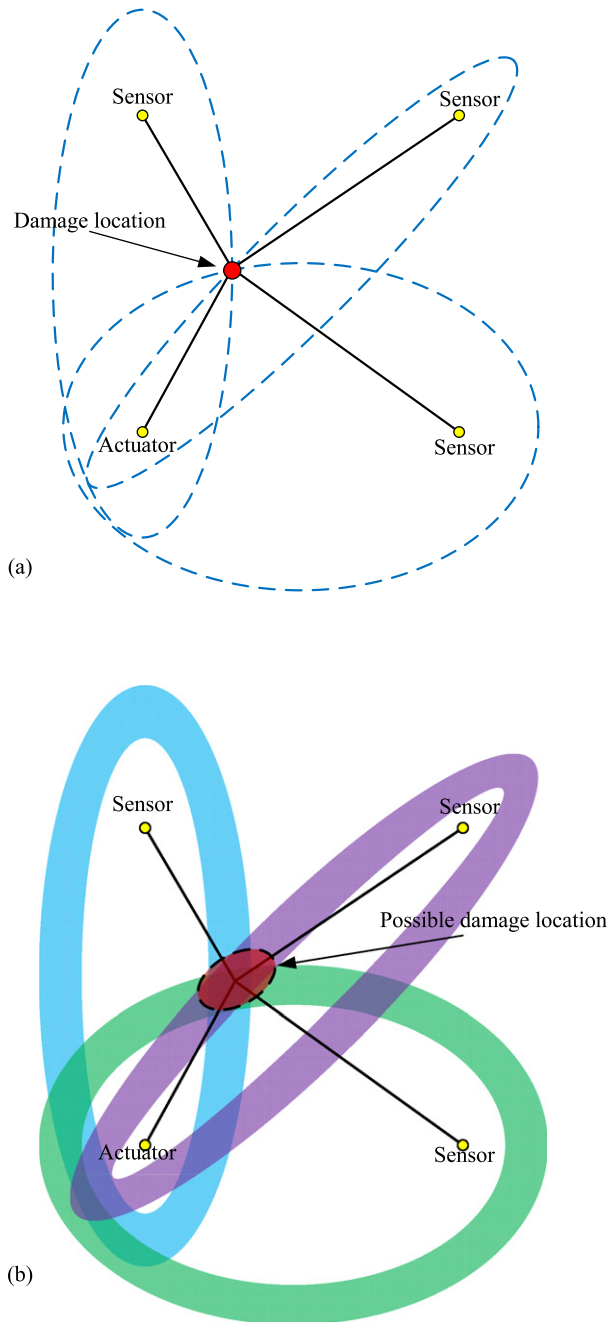
Figure 1. Damage localization using the ToF-based ellipse method. (a) Without uncertainty and (b) with uncertainty.

which all three loci intersect is considered as the location of damage, while the points with which only two loci intersect are considered as pseudodamage locations. Lemistre *et al* [8] and Su *et al* [9] identified the damage location by solving a set of nonlinear equations describing the relationships among damage location, wave velocities and ToF. Lu *et al* [10] solved this set of equations using a nonlinear least squares Gauss–Newton optimization algorithm to locate the damage.

However, there is a prerequisite in these traditional ToF-based damage localization approaches. That is, all of the measured ToF values and the corresponding theoretical wave velocities are accurate. In reality, errors and uncertainties are

always unavoidable in the measurement and identification process. For example, the size and extent of the damage are unknown before identification, and its effect on wave scattering is uncertain, which in turn affects the theoretical prediction of the ToF of the scattered Lamb waves; also the sizes of the actuator and sensor are usually not considered in damage localization, which may introduce error in the identification result. In addition, due to the dispersive nature of Lamb waves, the waveforms of the scattered waves are always distorted, affecting the accuracy of the ToF measurement. Depending on the ToF measurement method, the measured ToF values may be different. A variety of methods for increasing the accuracy of ToF measurement of Lamb waves have been developed, including short-time Fourier transform (STFT), Wigner–Ville distribution (WVD), continuous wavelet transform (CWT), Hilbert–Huang transform (HHT) and matching pursuit (MP) algorithm [11, 12, 7, 5] approaches. Nonetheless, as pointed out by Niri and Salamone in a recent paper [13], even by employing CWT which has good resolution both in time and frequency domains, systematic uncertainty could exist due to the Heisenberg uncertainty principle. Besides, uncertainties may arise from the theoretical wave velocities, since they depend on the material property values of a specific structure, which may have variations from those nominal values and be influenced by several factors, such as environmental temperature changes [14]. As a result, rather than the damage being located in a single point, it can be located anywhere in the dark overlapped region as shown in figure 1(b).

Under such a situation, probabilistic approaches may be more appropriate than deterministic approaches for damage localization in that probability distributions can be used to quantify the various uncertainties. Zhao *et al* [15] introduced probabilistic analysis into a tomography-based damage imaging method to improve the damage localization performance of the Lamb wave-based method. This probabilistic imaging method has been extended to complex structures and structures with multiple damaged areas [16, 17]. Flynn *et al* [18] proposed a maximum *a posteriori* probability (MAP) estimation method to increase the probability of damage detection and localization. Su *et al* [19–21] introduced a probability density function (PDF) to retrofit the traditional damage localization way in the ToF-based method. For each loci, a probability distribution map can be given for the detection target plant structure based on the PDF of damage occurrence. Combination of all the probability distribution maps can give the final damage detection result. Recently, Niri and Salamone proposed a probabilistic approach for acoustic emission damage localization in plate-like structures based on an extended Kalman filter (EKF) approach. The main advantage of the EKF algorithm over traditional methods is that it can take into account uncertainties in the ToF measurement and wave velocity [13].

The aim of this work is to apply the Bayesian system identification approach to the damage localization problem using the measured ToF of the scattered Lamb waves, while considering the uncertainties from modeling
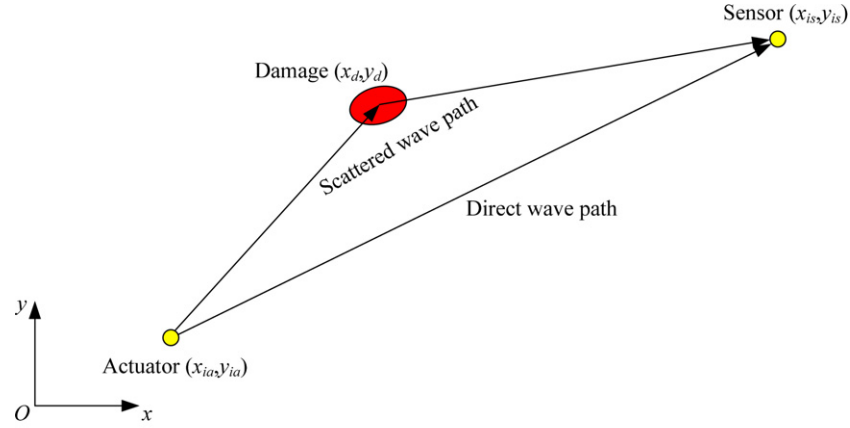
Figure 2. ToF calculation model for the scattered Lamb wave in the *i*th actuator–sensor path.

and measurement. The rest of this paper is structured as follows. Section 2 describes the proposed Bayesian approach for damage localization using scattered Lamb waves. Section 3 outlines the main characteristics of the CWT for measuring the ToF using a complex Morlet wavelet. In section 4, an introduction of the Markov chain Monte Carlo (MCMC) method and its application in sampling the posterior distribution of unknown parameters is presented. A numerical study for an aluminum plate and experimental studies for a stiffened aluminum panel and a composite laminate are presented in sections 5 and 6, respectively, to validate the proposed damage localization approach. Final conclusions are given in section 7.

2. Bayesian approach for ToF-based damage localization

The Bayesian framework in which measured data can be used to update the belief in the identification results, has previously been established and applied to structural systems by Beck and his colleagues [22–25]. One outstanding advantage of the Bayesian approach is that engineering judgments or expert knowledge can be easily incorporated into the analysis as prior information to reduce uncertainty. With the development of probabilistic methods to consider the intrinsic uncertainties of engineering structures, Bayesian approaches have played more and more important roles in SHM. It has been employed for damage assessment [26], damage prediction [27], sensor placement optimization [28], optimal SHM system design [29] and etc.

The present study employs Bayesian system identification for localizing damage based on the ToF of scattered Lamb waves. Rather than pinpointing a single solution using deterministic approaches, the Bayesian approach can provide the PDF of the unknown parameters, giving both point and interval estimates [30, 31]. The basic idea of Bayesian system identification is that it treats the parameters, usually denoted by a vector $\boldsymbol{\theta}$, as random variables with joint distribution $p(\boldsymbol{\theta})$. It aims to calculate the posterior (updated) distributions of

the uncertain parameters for a given set of measured data. The final parameter estimate can be taken as the mean value of the posterior or the value that maximizes the posterior distribution.

For plate-like structures, consider a sensor network consisting of N_p actuator–sensor paths that can excite and receive Lamb waves. In the present study, the ToF of the Lamb wave scattered by damage in the *i*th ($i = 1, 2, \ldots, N_p$) actuator–sensor path is defined as the total time for the Lamb wave to pass from the actuator to the damage and to the sensor. Figure 2 is an illustration of a simple model for calculating the ToF of the scattered wave in the *i*th actuator–sensor path. This model is widely used in ToF-based damage localization in Lamb wave-based methods. Theoretically, the calculated ToF in the *i*th actuator–sensor path T_i^c is defined as

$$T_i^c = \frac{\sqrt{(x_d - x_{ia})^2 + (y_d - y_{ia})^2}}{V_g(f)}$$
$$+ \frac{\sqrt{(x_d - x_{is})^2 + (y_d - y_{is})^2}}{V_g(f)} \quad (1)$$

where (x_d, y_d), (x_{ia}, y_{ia}), and (x_{is}, y_{is}) are the coordinates of the center location of damage, actuator, and sensor in the *i*th actuator–sensor path, respectively. V_g is the wave velocity of the scattered Lamb wave at a specific excitation frequency f. In equation (1), the sizes of the actuator, sensor and area of damage are not considered. Since uncertainties from material properties may influence the accuracy of the theoretical wave velocity value, in the present study, wave velocity V_g in equation (1) is set as an additional unknown parameter to be identified besides the coordinate of the damage center location (x_d, y_d), rather than calculated using the nominal material property values beforehand. Thus, the unknown parameter vector in this damage localization approach is $\boldsymbol{\theta} = [x_d, y_d, V_g]^T$. In the following part of this paper, θ_k ($k = 1, 2, 3$) is used to indicate the unknown parameters in $\boldsymbol{\theta}$ for convenience.

After the unknown parameters are defined, damage localization is formulated as a parameter identification

problem to be solved from a probabilistic point of view. Assume the modeling error and measurement uncertainty are described by two variables ε_1 and ε_2, respectively. The probabilistic description of the measured ToF in the ith actuator–sensor path T_i^{m} can be expressed as

$$T_i^{\mathrm{m}} = T_i^{\mathrm{c}}(\boldsymbol{\theta}) + \varepsilon_1 + \varepsilon_2, \tag{2}$$

where T_i^{c} is the calculated ToF in the ith actuator–sensor path using equation (1), with parameter vector $\boldsymbol{\theta}$. For simplicity and convenience, ε_1 and ε_2 are usually assumed as two independent Gaussian variables with means of zero and standard deviations of σ_{ε_1} and σ_{ε_2}, respectively. In this case, the likelihood function can be written as

$$p(\mathbf{D} \mid \boldsymbol{\theta}, \sigma_\varepsilon^2) = \frac{1}{(2\pi\sigma_\varepsilon^2)^{N_{\mathrm{p}}/2}}$$
$$\times \exp\left[-\frac{1}{2\sigma_\varepsilon^2}\sum_{i=1}^{N_{\mathrm{p}}}(T_i^{\mathrm{m}} - T_i^{\mathrm{c}}(\boldsymbol{\theta}))^2\right] \tag{3}$$

where the variance $\sigma_\varepsilon^2 = \sigma_{\varepsilon 1}^2 + \sigma_{\varepsilon 2}^2$. The likelihood function $p(\mathbf{D} \mid \boldsymbol{\theta}, \sigma_\varepsilon^2)$ is a probabilistic statement about the distribution of the measured ToF data $\mathbf{D} = [T_1^{\mathrm{m}}, T_2^{\mathrm{m}}, \ldots, T_{N_{\mathrm{p}}}^{\mathrm{m}}]$ given the predicted ToF values, determined by equation (1) and parameter vector $\boldsymbol{\theta}$. For convenience, the sum of squares in the likelihood function in equation (3) can be defined as

$$Q(\mathbf{D}, \boldsymbol{\theta}) = \sum_{i=1}^{N_{\mathrm{p}}}(T_i^{\mathrm{m}} - T_i^{\mathrm{c}}(\boldsymbol{\theta}))^2. \tag{4}$$

Using Bayes' theorem, the posterior PDF of the parameters for a given set of measured ToF data is constructed by relating the prior PDF and the likelihood function as

$$p(\boldsymbol{\theta}, \sigma_\varepsilon^2 \mid \mathbf{D}) = \frac{p(\mathbf{D} \mid \boldsymbol{\theta}, \sigma_\varepsilon^2)p_\pi(\boldsymbol{\theta}, \sigma_\varepsilon^2)}{p(\mathbf{D})} \tag{5}$$

where $p(\boldsymbol{\theta}, \sigma_\varepsilon^2 \mid \mathbf{D})$ is the joint posterior distribution of $\boldsymbol{\theta}$ and σ_ε^2, $p_\pi(\boldsymbol{\theta}, \sigma_\varepsilon^2)$ is the joint prior distribution of $\boldsymbol{\theta}$ and σ_ε^2, and

$$p(\mathbf{D}) = \int p(\mathbf{D} \mid \boldsymbol{\theta}, \sigma_\varepsilon^2)p_\pi(\boldsymbol{\theta}, \sigma_\varepsilon^2)\,\mathrm{d}\boldsymbol{\theta}\,\mathrm{d}\sigma_\varepsilon^2 \tag{6}$$

is a normalizing constant that ensures the integration of the PDF over the predefined domain is equal to unity. For each parameter θ_k, the marginal posterior distribution can be obtained by integrating equation (6) with respect to the rest of the parameters and variance σ_ε^2 over the domain of interest as

$$p(\theta_k \mid \mathbf{D}) = \int p(\boldsymbol{\theta}, \sigma_\varepsilon^2 \mid \mathbf{D})\mathrm{d}\boldsymbol{\theta}_{-k}\,\mathrm{d}\sigma_\varepsilon^2$$
$$\propto \int p(\mathbf{D} \mid \boldsymbol{\theta}, \sigma_\varepsilon^2)p_\pi(\boldsymbol{\theta}, \sigma_\varepsilon^2)\mathrm{d}\boldsymbol{\theta}_{-k}\,\mathrm{d}\sigma_\varepsilon^2 \tag{7}$$

where the notation $\int \mathrm{d}\boldsymbol{\theta}_{-k}\,\mathrm{d}\sigma_\varepsilon^2$ denotes the multidimensional integral over σ_ε^2 and all the remaining parameters other than θ_k in $\boldsymbol{\theta}$.

Equation (7) gives a general expression of the updated marginal PDF for each parameter in $\boldsymbol{\theta}$ using measured ToF data. After that, the parameters can be estimated for the posterior PDF, and damage location and wave velocity can

be identified. However, it is usually difficult to obtain an analytical solution of equation (7) since it involves integration over multidimensional parameters. In the present study, a MCMC sampling method is employed for drawing the posterior distributions for the parameters.

3. Measurement of ToF using CWT

As aforementioned, CWT has good resolution both in time and frequency domains, and it is popular in analyzing dispersive stress waves [11–13, 32]. Theoretically, a wavelet is a waveform with a limited duration or window, whose average amplitude equals zero. In CWT, a signal is redefined using dual parameters, scale parameter a defining the support width of the wavelet and translation parameter b localizing the wavelet in the time domain. The CWT of a signal $s(t)$ is defined by

$$\mathrm{CWT}(a, b) = \frac{1}{\sqrt{a}}\int_{-\infty}^{\infty} s(t)\psi^*\left(\frac{t-b}{a}\right)\mathrm{d}t \tag{8}$$

where $\mathrm{CWT}(a, b)$ is the CWT coefficient and the superscript $*$ denotes a complex conjugation. The kernel function in the CWT

$$\psi_{a,b}(t) = \frac{1}{\sqrt{a}}\psi\left(\frac{t-b}{a}\right) \tag{9}$$

is generated by simply scaling and shifting the mother wavelet $\psi(t)$ with a and b, respectively. In the present study, a complex Morlet wavelet is employed to determine the ToF of the scattered Lamb wave in the frequency of interest, as it is able to separate amplitude and phase information, enabling the measurement of instantaneous frequencies and their temporal evolution. Also, the complex Morlet wavelet enables the measurement of the localization frequency for signals with faster and slower oscillations, providing a flexible window that narrows at high frequencies and widens when observing low-frequency phenomena [13, 32].

The complex Morlet wavelet is expressed by the following equation

$$\psi(t) = \frac{1}{\sqrt{\pi f_{\mathrm{b}}}}\exp(-t^2/f_{\mathrm{b}})\exp(2\pi f_{\mathrm{c}}jt) \tag{10}$$

where f_{c} and f_{b} represent the center frequency and frequency bandwidth, respectively. f_{b} controls the shape of the mother wavelet and, for a given scale parameter a, it determines the resolution in time and frequency domains.

For CWT, the squared modulus, also called the scalogram, indicates the energy density of the signal in the time–frequency domain [33]. It is able to reveal the highest local energy content of the waveform measured from each sensor. The squared modulus can be expressed as

$$|\mathrm{CWT}(a, b)|^2 = \mathrm{CWT}(a, b) \cdot \mathrm{CWT}^*(a, b). \tag{11}$$

The maximum value of the coefficients of the scalogram with a high concentration of energy is achieved at the instantaneous frequency, corresponding to the dominant frequency in the signal analyzed at each instant in time.

These coefficients, taken at the instantaneous frequency in a time–frequency domain, determine the ridges. The projection on the time domain of the ridge corresponds to the time-of-arrival (ToA) of the scattered Lamb waves. Once the ToA is known, the ToF value can be determined. For analyzing scattered Lamb waves using the complex Morlet wavelet, each frequency of interest is related to the scale parameter by the following relationship

$$f = \frac{f_c}{a} f_s \qquad (12)$$

where f is the frequency of interest of the scattered Lamb wave for damage localization, f_c is the center frequency of the wavelet used and f_s is the sampling frequency of the scattered wave signal.

4. Markov chain Monte Carlo method

Posterior distributions used in Bayesian inference are often complicated, making it difficult to draw independent samples for the standard Monte Carlo method. In this case, MCMC simulation is usually employed as an alternative choice for sampling. The result of MCMC is a dependent sequence of samples (a Markov chain) that has stationary distributions equal to the target distribution.

The pioneering work on MCMC was done by Metropolis and his colleagues in the 1950s. They recognized that Markov chains could be applied to some difficult sampling problems. After about two decades, Hastings expanded and formalized MCMC into the procedure now known as the Metropolis–Hastings (MH) algorithm for performing such sampling [34]. Let $\pi(x)$ be the target PDF from which random samples are desired. The MH algorithm generates a sequence of $\{x^n\}$ for the target distribution $\pi(x)$ by a two-step rejection sampling procedure. At stage n, a candidate value x^* is sampled based on the current value $x^{(n-1)}$; it is sampled from a chosen proposal distribution function $h(x^* \mid x^{(n-1)})$. A Bernoulli trial is performed with success probability $\min\{\frac{\pi(x^*)h(x^{(n-1)}|x^*)}{\pi(x^{(n-1)})h(x^*|x^{(n-1)})}, 1\}$; if the result of the trial is success, $x^{(n)}$ is set to x^*, otherwise $x^{(n)}$ is kept to $x^{(n-1)}$. This process is repeated for a sufficient number of iterations, until the resulting Markov chain is stationary. Usually, when starting from an arbitrary state, there is a non-stationary period of iterations before the chain gets stationary. It is called the 'burn-in' period and should be discarded in the final representation of the posterior distribution. The proposal distribution could be an arbitrary distribution specified by the user, but proper ones can lead to better convergence in the resulting Markov chain. Often, symmetrical proposal distribution, which means $h(x^* \mid x^{(n-1)})$ is equal to $h(x^{(n-1)} \mid x^*)$, is used to simplify the acceptance probability as $\min\{\frac{\pi(x^*)}{\pi(x^{(n-1)})}, 1\}$. In particular, a widely used symmetrical transition distribution is the uniform distribution $h(x^* \mid x^{(n-1)}) = U(x^{(n-1)} - L, x^{(n-1)} + L)$, where $U(x_l, x_u)$ is a uniformly distributed number on $[x_l, x_u]$, meaning x^* is uniformly sampled from an interval of $2L$ centered on $x^{(n-1)}$.

In the present study, a MCMC algorithm for Gaussian likelihood and uniform transition distribution developed by Nichols *et al* [35, 36] is employed to sample the posterior distributions of the unknown parameters in $\boldsymbol{\theta}$ defined in section 2. Compared to the standard MH algorithm, this algorithm combines the Gibbs sampling concept that the full conditional distribution of each parameter can be thought of as its posterior distribution if other parameters' values are known. It updates each parameter sequentially by using the most recent sampled values. Also, in this algorithm, for each parameter, the interval $2L$ has been continuously tuned during the 'burn-in' period to achieve an appropriate acceptance rate and improve the performance of MCMC. In addition, it assumes a diffuse gamma prior on the precision parameter $1/\sigma_\varepsilon^2$ which is the case of conditional conjugacy; thus, the variance σ_ε^2 can be directly sampled from an inverse gamma distribution.

The employed MCMC algorithm for generating the posterior parameter distributions $p(\theta_k)$ for $\boldsymbol{\theta}$ given the ToF calculation model expressed in equation (1), the ToF data $\mathbf{D}$ measured by CWT, and prior parameter distributions $p_\pi(\theta_k)$ is performed in following steps:

Step 1. Set the number of total iterations N_T and the number of 'burn-in' iterations N_B.

Step 2. Initialize the chain with iteration number $n = 0$, initial values for each parameter (randomly chosen from the priors) $\boldsymbol{\theta}(0) = [\theta_1(0), \theta_2(0), \theta_3(0)]^T$ and for tuning parameters L_k ($k = 1, 2, 3$), initial variance $\sigma_\varepsilon^2(0)$ sampled from $\text{IG}(N_p/2 + 1, Q(\mathbf{D}, \boldsymbol{\theta}(0))/2)$, where $\text{IG}(\alpha, \beta)$ is an inverse gamma distribution with parameters α and β, and $Q(\mathbf{D}, \boldsymbol{\theta})$ is the sum of squares in the likelihood function defined in equation (4).

Step 3. Increase n by 1, and update the parameters one by one. For each parameter θ_k generate a candidate $\theta_k^* = \theta_k(n-1) + 2L_k \times U(-1, 1)$, compute $r = \frac{p_\pi(\boldsymbol{\theta}^*)}{p_\pi(\boldsymbol{\theta}(n-1))} \exp(-\frac{\sigma_\varepsilon^2(n-1)}{2} \times (Q(\mathbf{D}, \boldsymbol{\theta}^*) - Q(\mathbf{D}, \boldsymbol{\theta}(n-1))))$ where
$\boldsymbol{\theta}^* = [\theta_1^*, \theta_2(n-1), \theta_3(n-1)]^T$ and $\boldsymbol{\theta}(n-1) = [\theta_1(n-1), \theta_2(n-1), \theta_3(n-1)]^T$ when $k = 1$,
$\boldsymbol{\theta}^* = [\theta_1(n), \theta_2^*, \theta_3(n-1)]^T$ and $\boldsymbol{\theta}(n-1) = [\theta_1(n), \theta_2(n-1), \theta_3(n-1)]^T$ when $k = 2$,
$\boldsymbol{\theta}^* = [\theta_1(n), \theta_2(n), \theta_3^*]^T$ and $\boldsymbol{\theta}(n-1) = [\theta_1(n), \theta_2(n), \theta_3(n-1)]^T$ when $k = 3$.

Randomly generate a number R from uniform distribution $U(0, 1)$, if $R < r$, set $\theta_k(n) = \theta_k^*$, and adjust tuning parameter $L_k = L_k \times 1.01$, else reject the new value, keep $\theta_k(n) = \theta_k(n-1)$, and adjust tuning parameter $L_k = L_k/1.07$.

Step 4. Directly sample the variance $\sigma_\varepsilon^2(n)$ from $\text{IG}(N_p/2 + 1, Q(\mathbf{D}, \boldsymbol{\theta}(n))/2)$.

Step 5. Repeat step 3 and step 4 until $n = N_T$ (after $n > N_B$ iterations, cease adjusting the tuning parameters L_k). Discard samples in the 'burn-in' period and record subsequent values $\theta_k(n)$ as members of stationary Markov chains that can represent the posterior distributions $p(\theta_k)$.
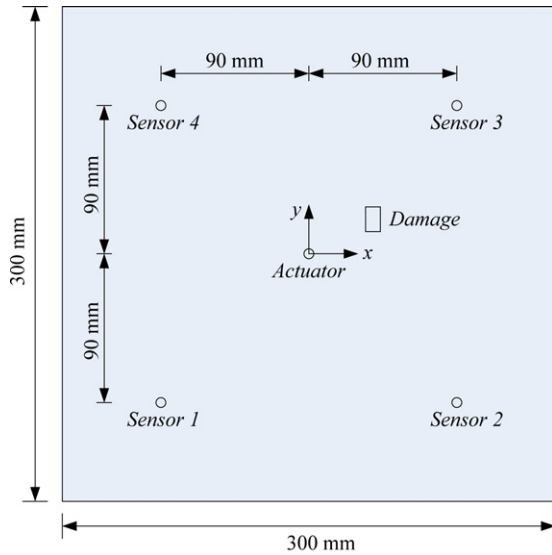
5. Numerical study

5.1. Finite element model

To illustrate the effectiveness of the proposed damage localization method, a numerical study for an aluminum plate

Table 1. Coordinates of the actuator, sensors and damage on the aluminum plate in the numerical study.
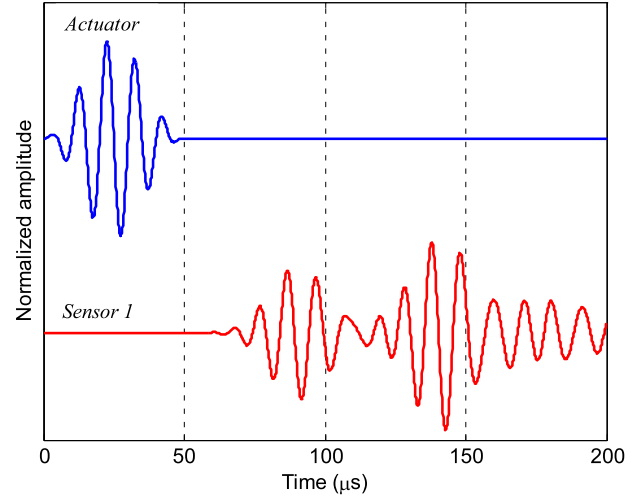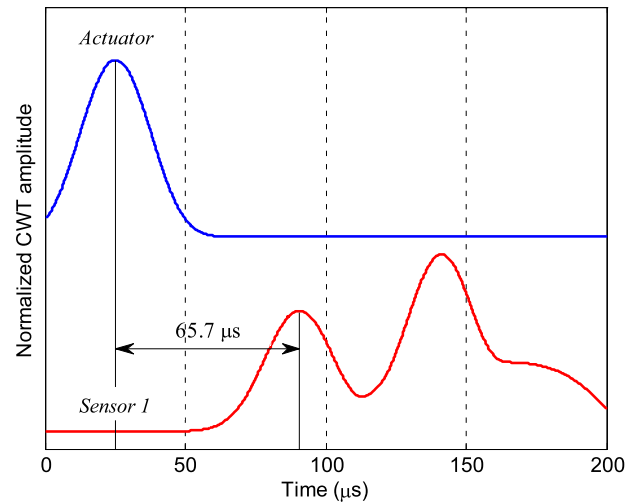
	Actuator	Sensor 1	Sensor 2	Sensor 3	Sensor 4	Damage
Coordinates (mm)	(0, 0)	(−90, −90)	(90, −90)	(90, 90)	(−90, 90)	(40, 20)

Figure 3. Layout of a square aluminum plate with an actuator, sensors and damage in the numerical study.

Figure 4. Excitation signal and wave signal received by sensor 1 under the undamaged state in the numerical study.

Figure 5. CWT of the excitation signal and wave signal received by sensor 1 under the undamaged state at 100 kHz in the numerical study.

is performed. The material properties of the aluminum plate are Young's modulus $E = 72$ GPa, Poisson ratio $v = 0.3$ and density $\rho = 2700$ kg m^{-3}. To generate the synthetic scattered Lamb waves, the commercial finite element package ABAQUS is used. An explicit central difference scheme is employed to obtain the responses of the plate.

As shown in figure 3, the size of the aluminum plate is 300 mm × 300 mm × 1.5 mm. The origin of the coordinate system is set at the center of the plate. Assume that one actuator and four sensors are configured on the plate, and the coordinates of the actuator and sensors are listed in table 1. A uniform square mesh of 1 mm × 1 mm is used and the element type is an S4R shell element [37, 38]. All of the boundaries are set as free in the model. Single rectangular through-hole damage is considered, and the center of the damage is located at (40, 20) mm. Three different sizes of 2 mm × 4 mm, 4 mm × 8 mm and 8 mm × 8 mm are considered to demonstrate the effect of damage size on damage localization.

In the numerical simulation, the actuator is subjected to a narrowband tone-burst five-cycle transverse excitation with a center frequency of 100 kHz. The excitation frequency is below the cut-off frequency of the A_1 mode Lamb wave, only the A_0 mode is excited. The scattered waves from the damage are obtained by subtracting the waves without damage from the total waves of the plate with damage. The excited and sensed signals are applied and obtained at corresponding nodes of the finite element model, respectively; thus, the sizes of the actuator and sensors are not considered.

5.2. Numerical results

Figure 4 shows the excitation signal and the sensed signal by sensor 1 under the undamaged state. A CWT of the complex Morlet wavelet is used to analyze the wave signals to obtain the ToF of the Lamb wave from the actuator to sensor 1. Figure 5 shows the magnitude of the CWT coefficients of the excitation and sensor 1 signal at a center frequency of 100 kHz. From the figure, the ToA can be easily determined by the first CWT peak, and the corresponding ToF for Lamb waves at 100 kHz are labeled in figure 5. The start point for
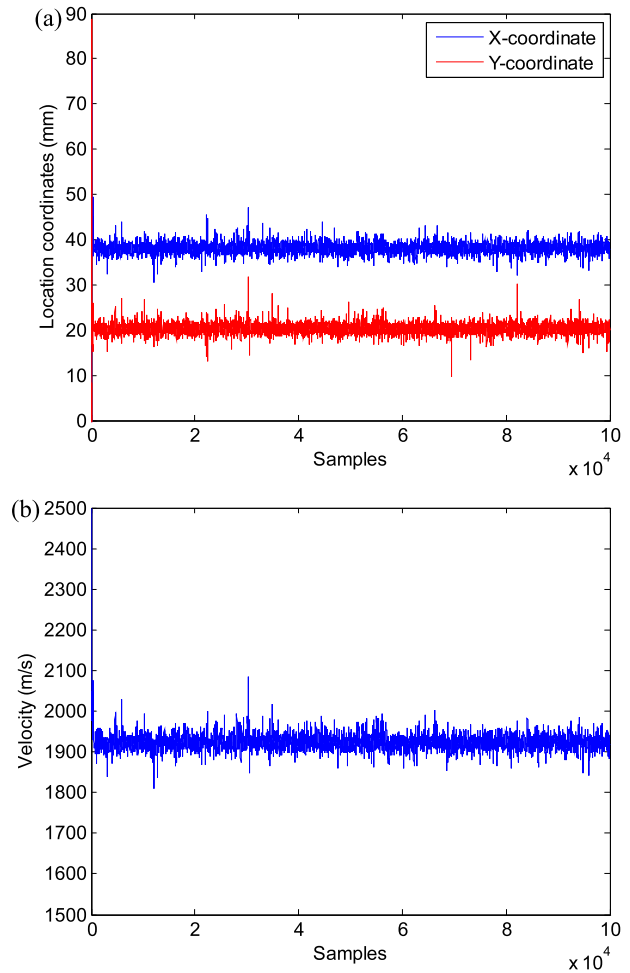
Table 2. CWT measured ToF without error in the numerical study.

Damage size	ToF (μs)			
	Actuator–sensor 1	Actuator–sensor 2	Actuator–sensor 3	Actuator–sensor 4
2 mm × 4 mm	110.1	86.1	67.5	98.6
4 mm × 8 mm	111.0	85.4	67.4	97.7
8 mm × 8 mm	109.8	82.9	67.1	94.7
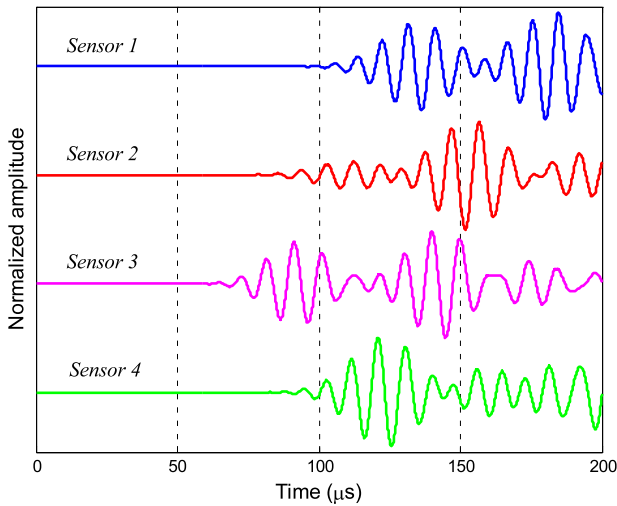
Figure 6. Scattered waves by damage with a size of 2 mm × 4 mm in the numerical study.
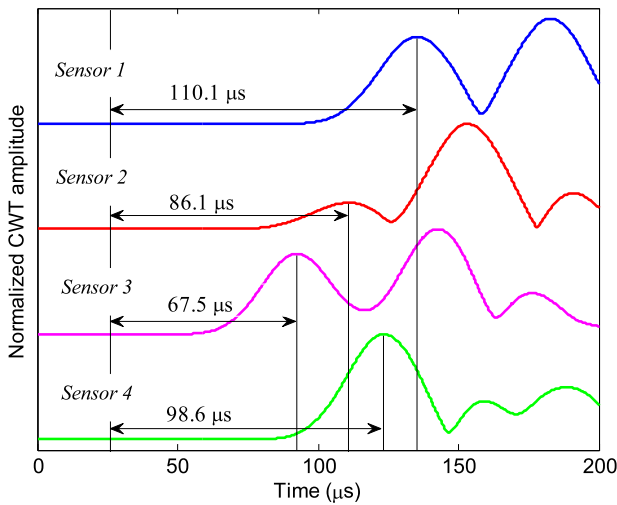
Figure 7. CWT of scattered waves by damage with a size of 2 mm × 4 mm at 100 kHz in the numerical study.

Figure 8. MCMC samples for damage with a size of 2 mm × 4 mm in the numerical study; (a) samples for coordinates of damage location and (b) samples for wave velocity at 100 kHz.

ToF measurement is 25 μs which corresponds to the CWT peak of the excitation signal. With the ToF value and the distance between the actuator and sensor 1, the propagation velocity of the A_0 mode Lamb wave at 100 kHz in this numerical simulation can be calculated as 1937 m s^{-1}. This value is used for reference after the MCMC identification results are obtained.

Figure 6 shows the wave signals scattered by the though-hole damage with size of 2 mm × 4 mm. Figure 7

shows the magnitude of the CWT coefficients of the scattered waves at a center frequency of 100 kHz, and the corresponding ToF for the scattered waves at 100 kHz from the actuator to the sensors are labeled in figure 7 and listed in table 2. The MCMC procedure described in section 4 is performed to identify the damage location and wave velocity. Uniform priors are assumed, i.e., the x–y coordinates of the center location of damage are uniformly distributed in $[-90, 90]$ mm, and the wave velocity is uniformly distributed in $[0, 3000]$ m s^{-1}. Figure 8(a) shows the samples of x–y coordinates of center location of damage by MCMC, and figure 8(b) shows the simultaneously sampled wave velocity of a scattered Lamb wave at 100 kHz. For each parameter, a total of 100 000 samples are obtained by MCMC in which
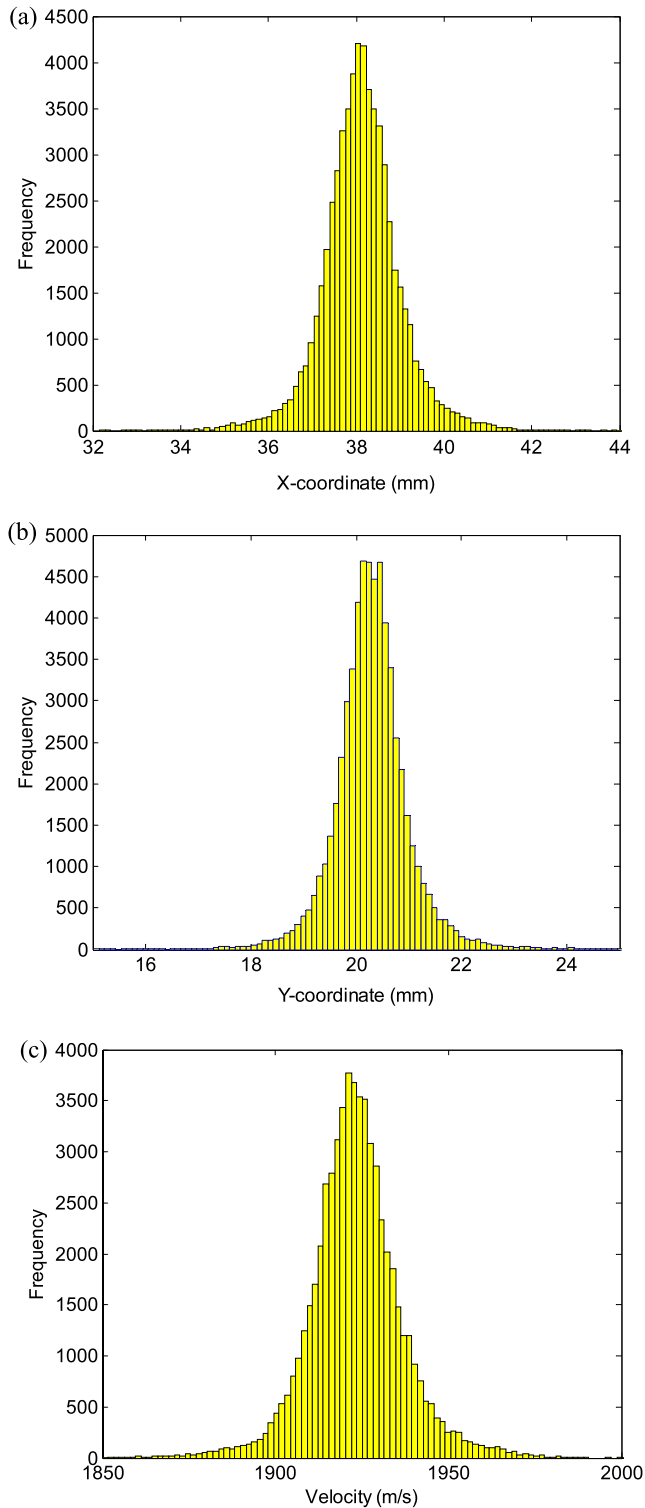
Figure 9. Histograms of MCMC samples for damage with a size of 2 mm × 4 mm in the numerical study; (a) x-coordinate (x_d), (b) y-coordinate (y_d) and (c) wave velocity (V_g).
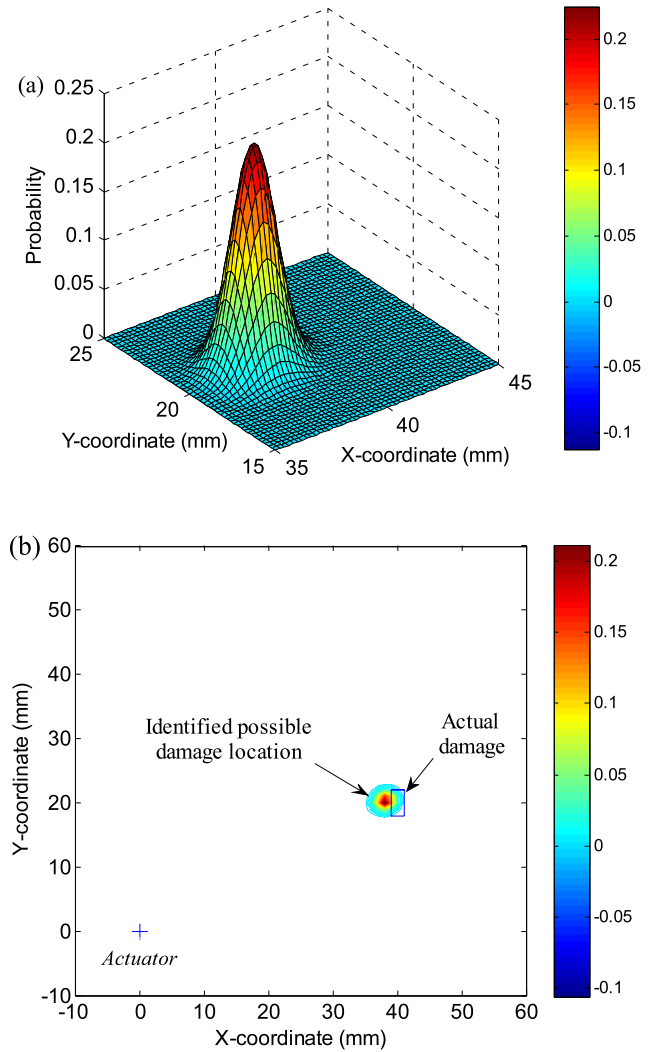

Figure 10. Joint PDF of the identified possible damage location for damage with a size of 2 mm × 4 mm in the numerical study. (a) 3D view and (b) 2D contour.

the first 40 000 are set as the 'burn-in' period. Figure 9 illustrates the histograms formed by the remaining 60 000 samples for each parameter. Normal distribution is employed to fit the histograms. Figure 10 illustrates the fitted joint PDF of the x–y coordinates of the center location of damage

in 3D and 2D views, respectively. The actual rectangular through-hole damage is also labeled in figure 10(b) for comparison. The final parameter estimates are taken as the means of the fitted normal distributions. The identified center location of damage is (38.1, 20.3) mm; the distance between the identified damage location and the actual center location is less than 2 mm. The identification results are listed in table 3.

Similar identification results are obtained for though-hole damage with sizes of 4 mm × 8 mm and 8 mm × 8 mm. The CWT measured ToF of scattered waves in these two damage cases is listed in table 2 and the identification results are listed in table 3 together with those for 2 mm × 4 mm through-hole damage. In table 3, the relative error for damage location is defined as the ratio of the distance between the identified location and the actual location with respect to the sensor spacing (180 mm in the numerical model); for wave velocity, it is defined as the ratio of the difference between identified and actual values with respect to the actual value. From table 3, it can be seen that the identified values are quite close

Table 3. Identified results by CWT measured ToF without error in numerical study.

Damage size	Coordinates of center location			Wave velocity		
	(x_d, y_d) (mm)	COV (%)	Error (%)	V_g (m s^{-1})	COV (%)	Error (%)
2 mm × 4 mm	(38.1, 20.3)	(2.3, 3.9)	1.1	1923.3	0.7	−0.7
4 mm × 8 mm	(39.1, 21.0)	(4.2, 5.7)	0.8	1940.7	1.3	0.2
8 mm × 8 mm	(39.0, 20.7)	(13.0, 18.7)	0.7	1982.3	4.0	2.3

Table 4. CWT measured ToF with error ($\eta = 2\%$) in the numerical study.

Damage size	ToF (μs)			
	Actuator–sensor 1	Actuator–sensor 2	Actuator–sensor 3	Actuator–sensor 4
2 mm × 4 mm	110.0	83.6	66.1	97.2
4 mm × 8 mm	113.9	85.1	67.3	100.1
8 mm × 8 mm	112.4	81.8	67.9	90.5
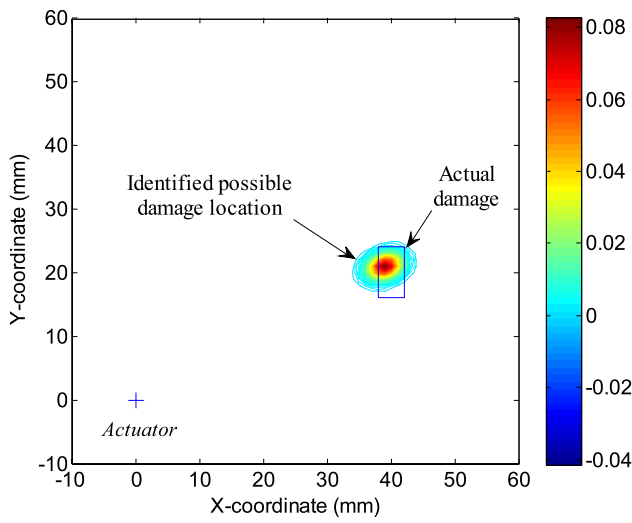
Figure 11. Joint PDF of identified possible damage location for damage with a size of 4 mm × 8 mm in the numerical study.
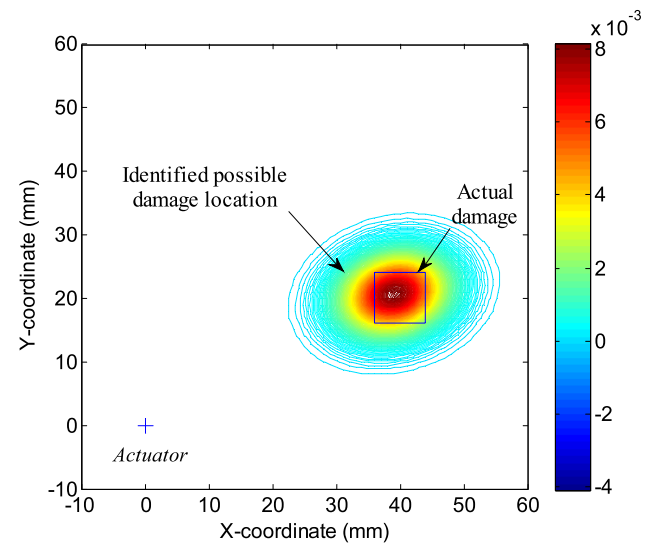
Figure 12. Joint PDF of identified possible damage location for damage with a size of 8 mm × 8 mm in the numerical study.

to the actual ones. The coefficient of variation (COV) which is defined as the ratio of the standard deviation to the mean of the fitted normal distribution for each identified parameter is also presented. The COV is a convenient way to analyze the uncertainty associated with a parameter. Figures 11 and 12 illustrate the fitted PDF of *x*–*y* coordinates of the center location of damage in 2D contours for damage with sizes of 4 mm × 8 mm and 8 mm × 8 mm, respectively. From these two figures and table 3, it is clear that the uncertainties associated with the identification results tend to increase as the damage size is increased.

Since the numerically obtained scattered wave signals are noise-free, the CWT measured ToF in table 2 is considered as sufficiently accurate. To consider the effect of uncertainties from instrumentation noise on the accuracy of ToF measurement, zero-mean Gaussian-type errors are directly added to the CWT measured ToF of the noise-free scattered wave signals. The ToF data with error T_i^{me} are generated as follows

$$T^{me} = T^m(1 + e) \tag{13}$$

where T^m is the CWT measured ToF for the noise-free scattered wave signals, and *e* is a Gaussian variable with zero mean and standard deviation η. The value of η controls the error level, and $\eta = 2\%$ is chosen in the present study. Table 4 lists the ToF data with error for randomly generated *e* with $\eta = 2\%$. Table 5 illustrates the identification results. Compared with table 3, it can be demonstrated that, as expected, for most of the cases the deviations between the identified damage locations and the actual ones increase, while uncertainties associated with the identification results increase too.

6. Experimental studies

6.1. Experimental set-up for stiffened aluminum panel

To further demonstrate the effectiveness of the proposed method, experimental studies for a stiffened aluminum panel and a composite laminate are conducted. For the stiffened aluminum panel, the test set-up consists of a KH-7600
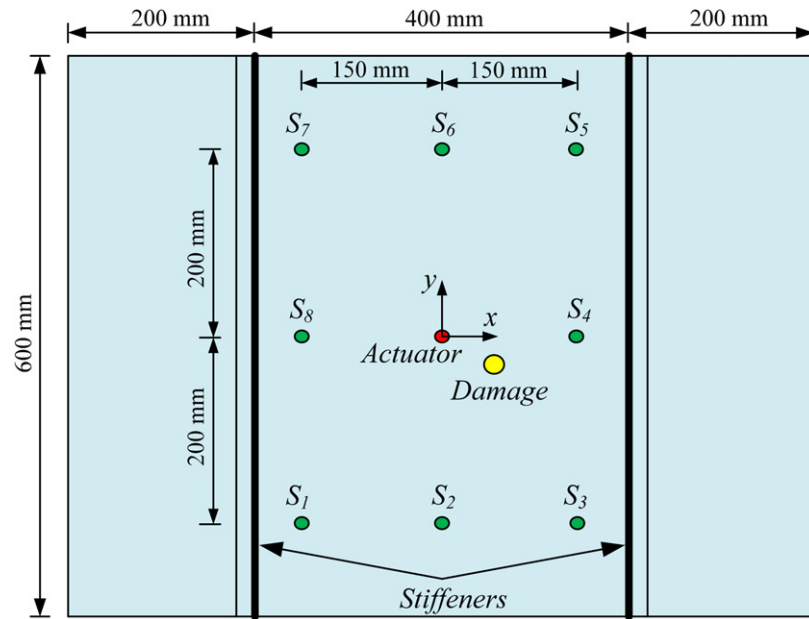
Figure 13. Test configuration and sensor arrangement for the stiffened aluminum panel.

Table 5. Identified results by CWT measured ToF with error ($\eta = 2\%$) in the numerical study.

Damage size	Coordinates of center location			Wave velocity		
	(x_d, y_d) (mm)	COV (%)	Error (%)	V_g (m s^{-1})	COV (%)	Error (%)
2 mm × 4 mm	(41.3, 20.8)	(4.3, 6.3)	0.9	1991.8	1.4	2.8
4 mm × 8 mm	(43.8, 21.2)	(7.8, 11.4)	2.2	1972.2	2.7	1.8
8 mm × 8 mm	(41.9, 25.2)	(35.6, 50.2)	3.1	2097.6	11.9	8.3

Table 6. Coordinates of the actuator, sensors and damage on the stiffened aluminum panel.

	Actuator	S_2	S_3	S_4	S_6	S_7	S_8	Damage
Coordinates (mm)	(0, 0)	(0, −200)	(150, −200)	(150, 0)	(0, 200)	(−150, 200)	(−150, 0)	(50, −30)

wideband amplifier, and a NI PXI system incorporated with a PXI-5441 arbitrary function generator and a PXI-5105 8-channel digitizer. The dimensions of the stiffened aluminum panel are 800 mm × 600 mm × 2 mm. A sensor network containing nine PZT transducers with a diameter of 10 mm and thickness of 1 mm are surface mounted on an area of 300 mm × 400 mm between two riveted stiffeners. One PZT in the center of the panel is used as the actuator, and others are used as sensors, denoted by S_1–S_8. Unfortunately, S_1 and S_5 malfunctioned in the following test, so only the remaining six sensors are employed for damage localization. An illustration of the stiffened panel and sensor placement is shown in figure 13. The origin of the coordinate system is set at the center of the actuator, and the coordinates of the actuator and sensors are listed in table 6. A steel nut with a diameter of 10 mm is used to mount on the surface of the panel to simulate damage effect. The center location of the simulated damage is at (50, −30) mm in the coordinate system.

In the experiment, the arbitrary function generator generates a narrowband tone-burst five-cycle signal, and applies it to the actuator after it is amplified by the wideband amplifier. The amplitude of the signal output by the function generator is 6 V and the gain of the amplifier is set at 28 dB. The center frequency of the excitation is 50 kHz, since a preliminary test on this panel has shown that in this frequency range, the signal is dominated by the A_0 mode Lamb wave. Therefore, it can be assumed that only a single A_0 mode wave exists. The response wave signals are then received by the sensors and acquired by the digitizer, whose sampling rate is set at 10 MHz.
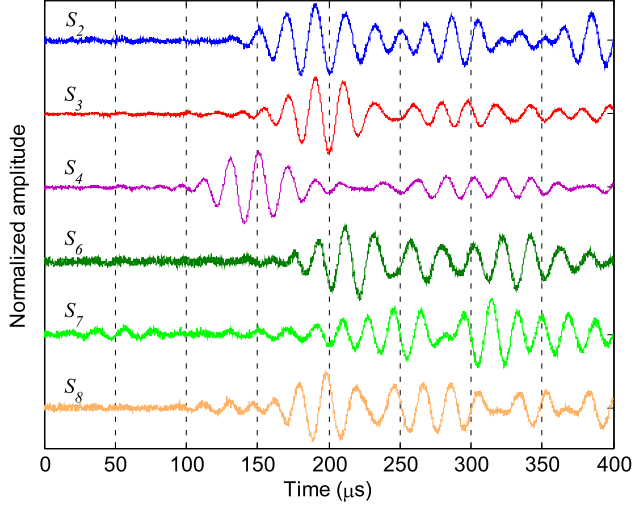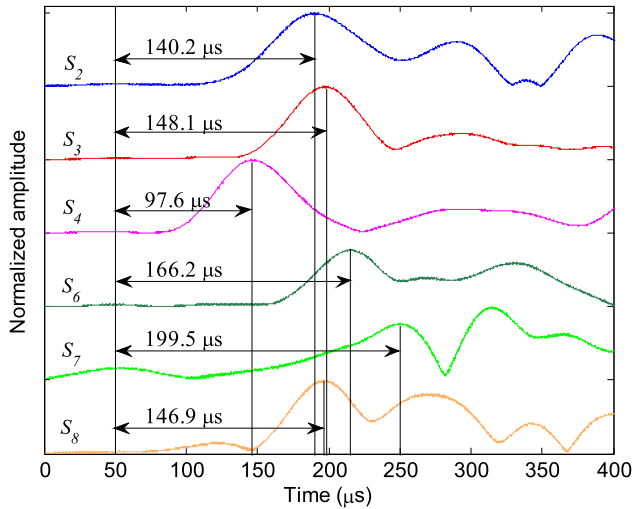
6.2. Experimental results for the stiffened aluminum panel

Figure 14 shows the wave signals scattered by the simulated damage received by the six sensors. As in the numerical study, a CWT of the complex Morlet wavelet is used to analyze the wave signals to obtain the ToF of the scattered waves. Figure 15 shows the magnitude of the CWT coefficients of the scattered waves at a center frequency of 50 kHz. The corresponding ToF for the scattered waves at 50 kHz are determined and labeled in figure 15 and listed in table 7. The start point for the ToF calculation is 50 μs, which corresponds to the peak of the CWT of the excitation signal.
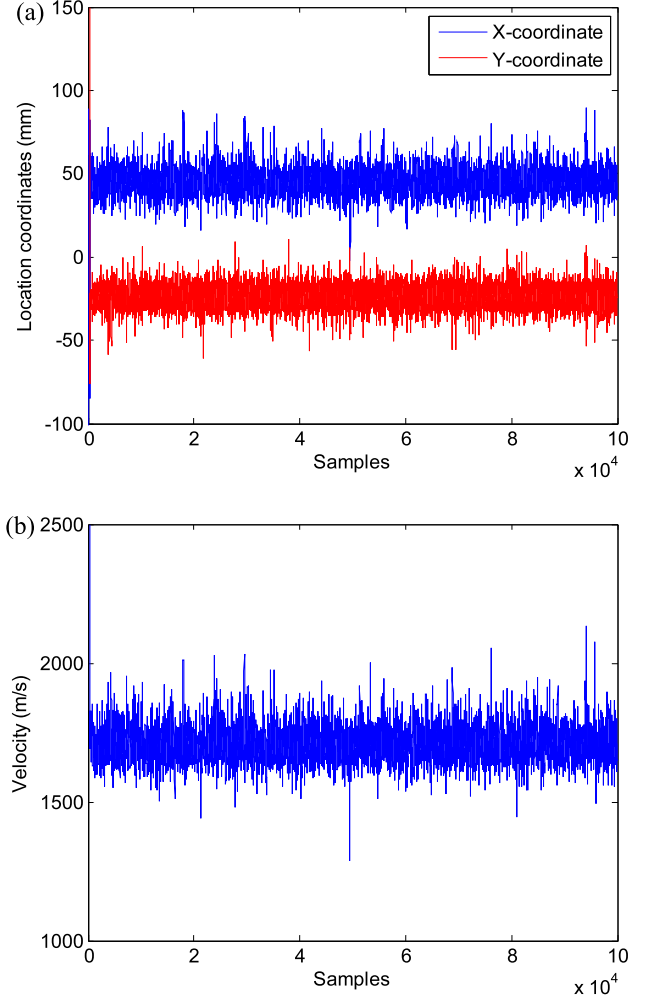
Similar to the numerical study, the MCMC procedure is then performed. For the initial values, the x-coordinate of

Table 7. CWT measured ToF in the experimental study for the stiffened aluminum panel.

	Actuator-S_2	Actuator-S_3	Actuator-S_4	Actuator-S_6	Actuator-S_7	Actuator-S_8
ToF (μs)	140.2	148.1	97.6	166.2	199.5	146.9

Figure 14. Scattered waves by damage in the experimental study for the stiffened aluminum panel.

Figure 15. CWT of scattered waves by damage at 50 kHz in the experimental study for the stiffened aluminum panel.

Figure 16. MCMC samples for damage in the experimental study for the stiffened aluminum panel. (a) Samples for coordinates of damage location and (b) samples for wave velocity at 50 kHz.

damage location is uniformly sampled from $[-150, 150]$ mm, the y-coordinate of damage location is uniformly sampled from $[-200, 200]$ mm, and the wave velocity is uniformly sampled from $[0, 3000]$ m s^{-1}. Figure 16(a) shows the samples of x–y coordinates of the center location of damage by MCMC, and figure 16(b) shows the simultaneously sampled wave velocity of the A$_0$ mode Lamb wave at 50 kHz. For each parameter, a total of 100 000 samples are obtained and the first 40 000 are set as the 'burn-in' period. Figure 17 shows the histograms formed by the remaining 60 000 samples for each parameter. Figures 18(a) and (b) illustrate

the fitted joint PDF of x–y coordinates of the center location of damage in 3D and 2D views, respectively. The simulated damage is also labeled in figure 18(b) for comparison. The identified center location of damage is $(45.4, -23.9)$ mm, the distance between the identified damage location and the actual center location is less than 7.64 mm with a relative error of 5.1% with respect to the minimum sensor spacing (150 mm), demonstrating the effectiveness of the proposed Bayesian localization approach. For the wave velocity, the identified value at 50 kHz is 1707.3 m s^{-1}, close to the averaged measured value 1731.2 m s^{-1} from the six actuator–sensor path under the undamaged state with a relative error of -1.4%.
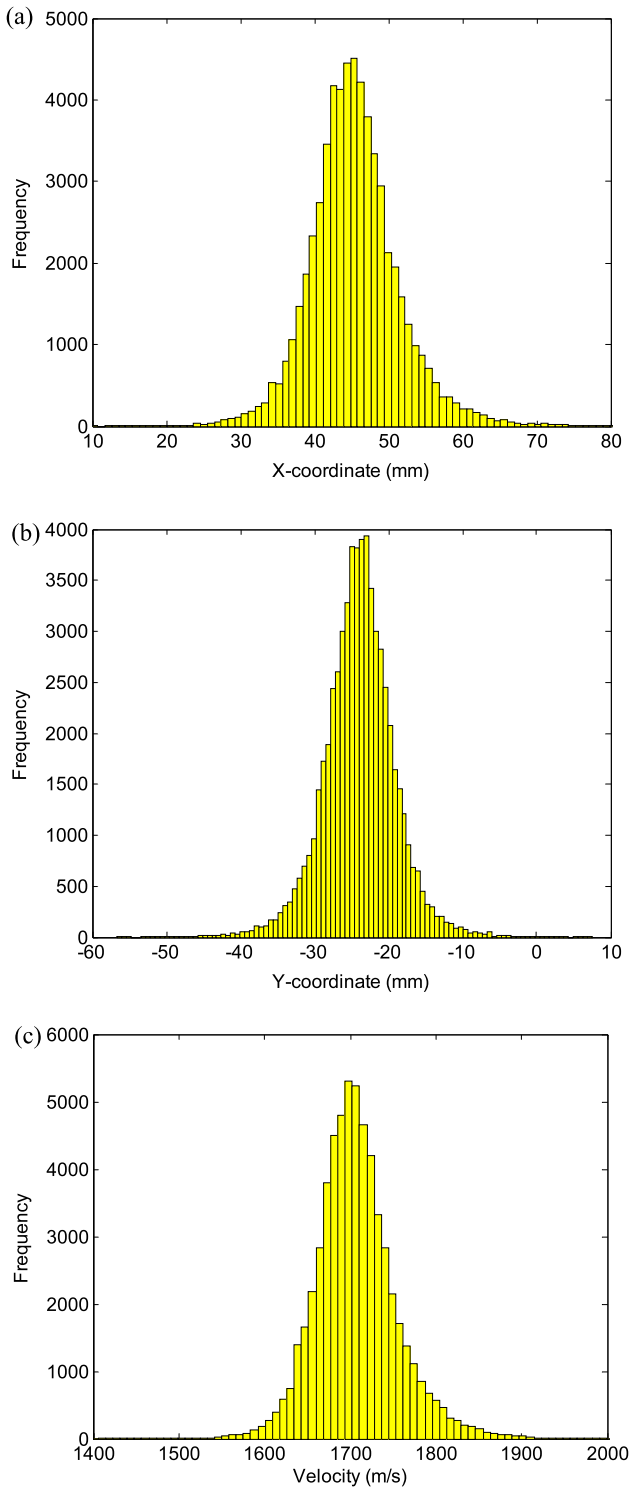
Figure 17. Histograms of MCMC samples for damage in the experimental study for the stiffened aluminum panel.
(a) x-coordinate (x_d), (b) y-coordinate (y_d) and (c) wave velocity (V_g).
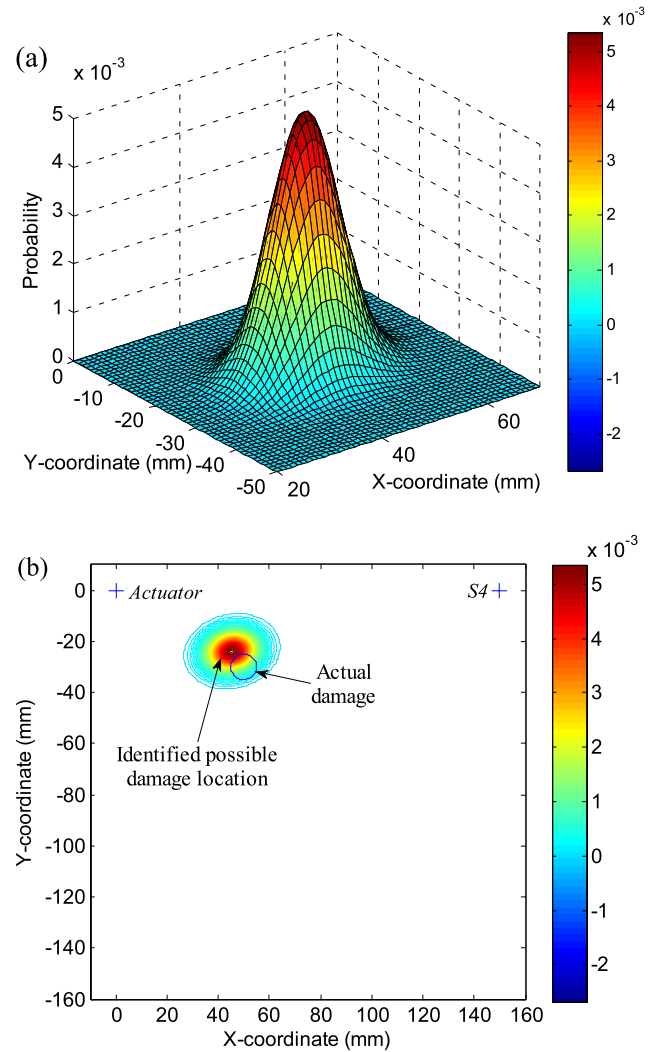

Figure 18. Joint PDF of identified possible damage location for damage in the experimental study for the stiffened aluminum panel. (a) 3D view. (b) 2D contour.

6.3. Experimental set-up for the composite laminate

For the composite laminate, the test set-up consists of a charge amplifier, a TDS-3012 digital oscilloscope and an NI PXI system incorporated with a PXI-5411 arbitrary function generator. The dimensions of the composite laminate are 400 mm $\times$ 300 mm $\times$ 3.2 mm. The lay-up of the laminate contains 27 plies stacked according to the sequence $[-45/45/0/45/0/-45/90/-45/0/45/0/45/0/-45_{1/2}]_s$, and consists of T300 graphite fibers and a QY8911 epoxy matrix. The sensor network contains four PZT transducers with a diameter of 10 mm and thickness of 1 mm, denoted by P_1, P_2, P_3 and P_4; the distance between the adjacent PZT sensors is 180 mm. An illustration of the composite laminate and sensor placement is shown in figure 19. The origin of the coordinates is set at the center of P_1 and the coordinates of sensors are listed in table 8. A steel nut with a diameter of 10 mm is used to mount on the surface of the laminate to simulate damage effect. The center location of the simulated damage is at (110, 45) mm in the coordinate system.

In the experiment, the arbitrary function generator generates a narrowband tone-burst five-cycle signal and applies it to one PZT sensor. The amplitude of the excitation signal is 10 V, and the center frequency is 50 kHz. In this frequency range, the excited wave in the test laminate is also

Table 8. Coordinates of sensors and damage on the composite laminate.

	P_1	P_2	P_3	P_4	Damage
Coordinates (mm)	(0, 0)	(180, 0)	(180, 180)	(0, 180)	(110, 45)

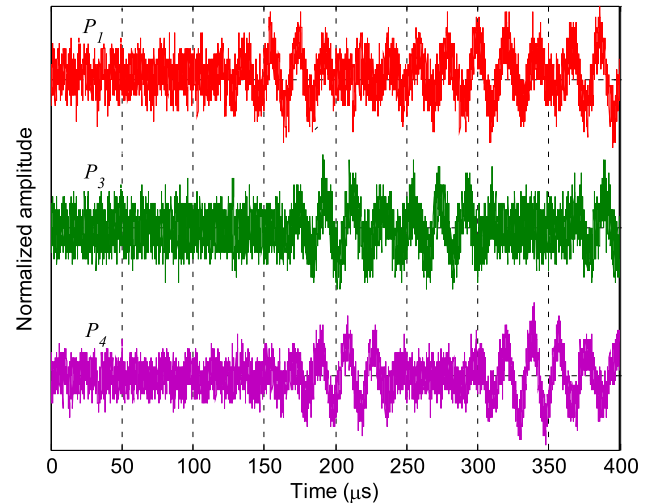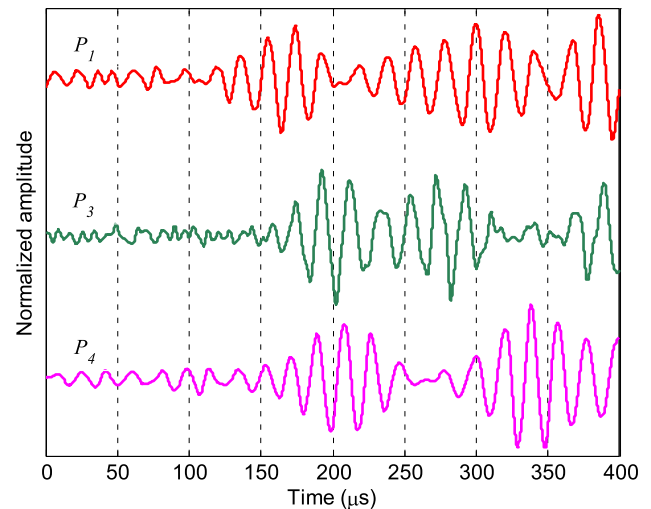**Table 9.** CWT measured ToF in the experimental study for the composite laminate.

	P_1–P_2	P_1–P_3	P_1–P_4	P_2–P_3	P_2–P_4	P_3–P_4
ToF (μs)	118.2	157.0	172.4	150.6	157.9	200.8
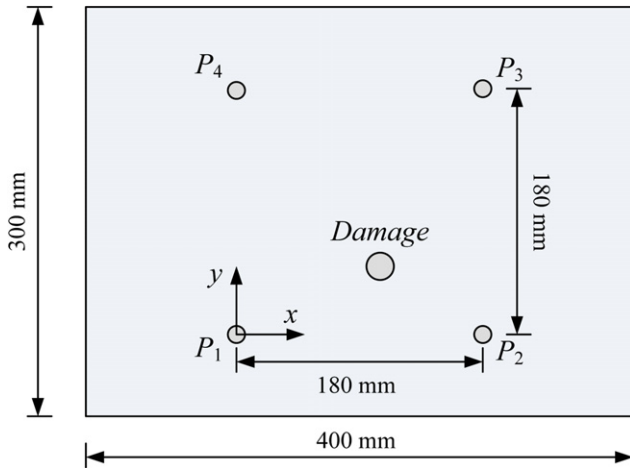
Figure 19. Test configuration of sensor arrangement for the composite laminate.

Figure 20. Scattered waves by damage in the experimental study for the composite laminate.

dominated by the A_0 mode Lamb wave. The response wave signals are then received by other sensors, amplified by the charge amplifier and acquired by the digital oscilloscope, whose sampling rate is set at 25 MHz. The four PZT sensors are individually actuated; as a result, responses in a total of twelve actuator–sensor paths are obtained. However, according to the reciprocal theory, only six actuator–sensor paths are different. The scattered waves in these six paths are used to identify the location of the simulated damage.

6.4. Experimental results for the composite laminate

Figure 20 shows the wave signals scattered by the simulated damage when P_2 is actuated by the excitation signal. As shown in the figure, due to low signal-to-noise ratio (SNR), the scattered wave signals are of the same order of magnitude as the noise. One appealing property of wavelet analysis is its powerful de-noising capability. After applying a discrete wavelet transform (DWT) to the raw scattered wave signals, the noises are effectively filtered as shown in figure 21. Figure 22 shows the magnitude of the CWT coefficients of the scattered waves at a center frequency of 50 kHz. The corresponding ToF for the scattered waves at 50 kHz are determined and labeled in figure 22. Table 9 gives the measured ToF values in the six different actuator–sensor paths for damage localization.

Figure 21. DWT-denoised scattered waves by damage in the experimental study for the composite laminate.

When applying the proposed damage localization approach to the test laminate, one assumption is made that the wave velocity is independent of the propagation angle to simplify the localization problem. Figure 23 is the theoretical velocity distribution of the A_0 Lamb wave for the test laminate
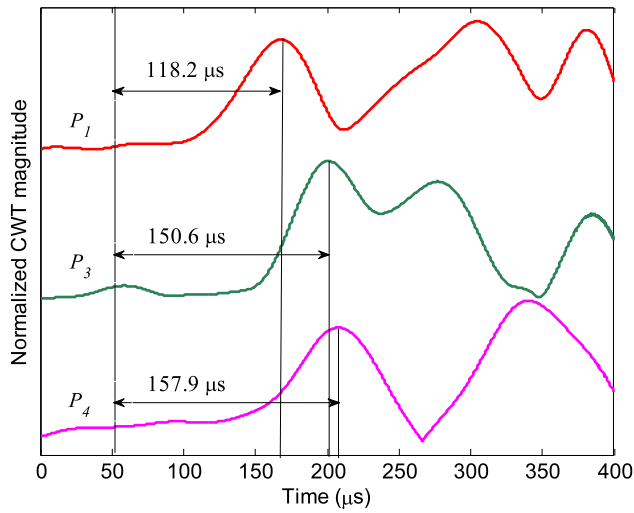
Figure 22. CWT of scattered waves by damage at 50 kHz in the experimental study for the composite laminate.
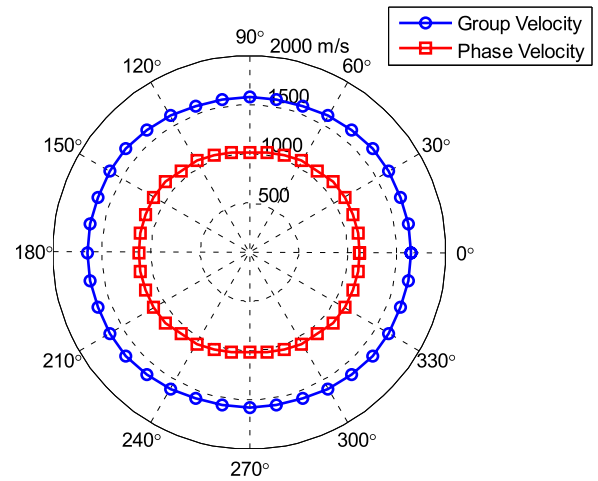

Figure 23. Theoretical velocity distribution of the A_0 mode Lamb wave of the composite laminate at 50 kHz.
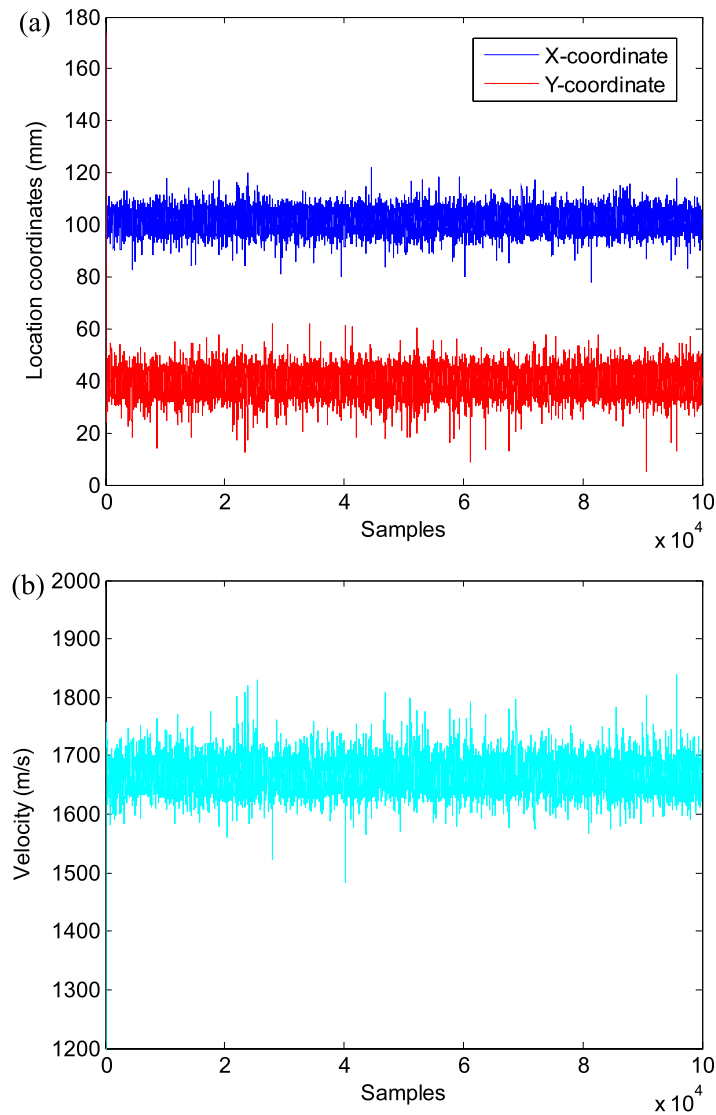

Figure 24. MCMC samples for damage in the experimental study for the composite laminate; (a) samples for coordinates of damage location and (b) samples for wave velocity at 50 kHz.
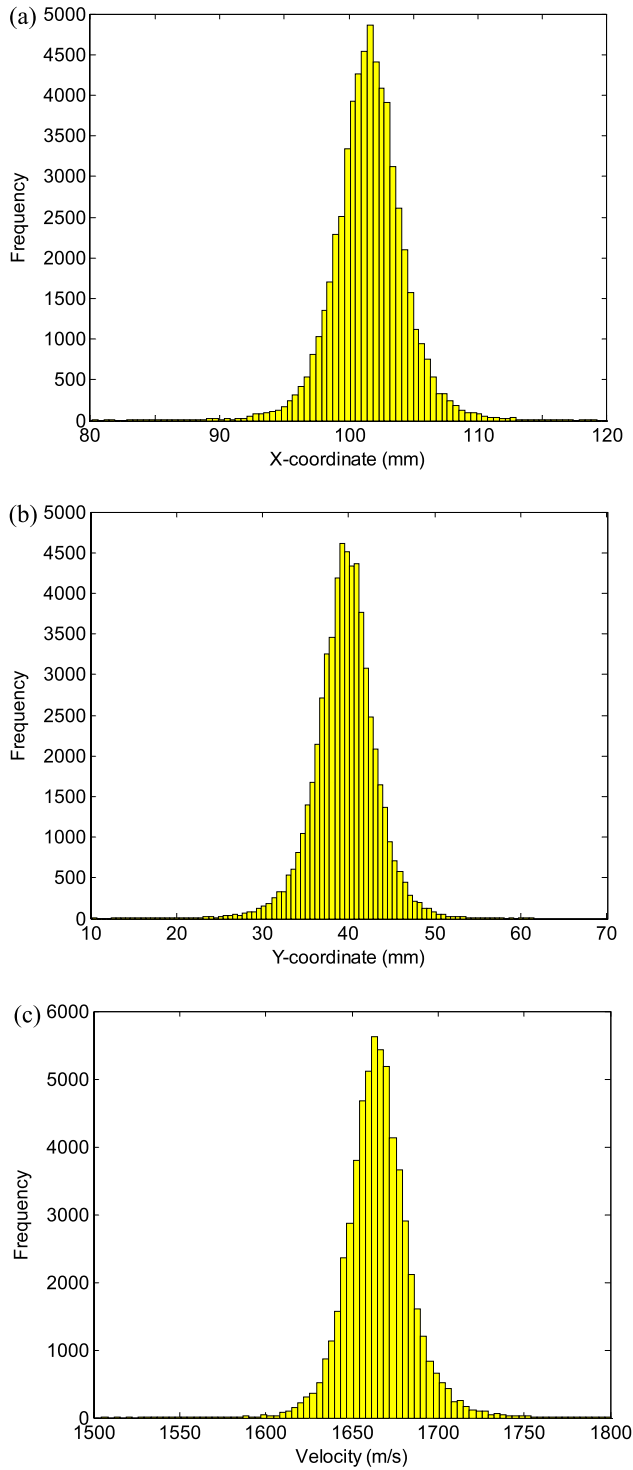
Figure 25. Histograms of MCMC samples for damage in the experimental study for the composite laminate; (a) x-coordinate (x_d), (b) y-coordinate (y_d) and (c) wave velocity (V_g).

Figure 26. Joint PDF of identified possible damage location for damage in the experimental study for the composite laminate. (a) 3D view and (b) 2D contour.

over the propagation angle at 50 kHz with the known nominal material properties. From the figure, it can be seen that at this frequency range, the wave velocity does not show strong directional dependence; the assumption is reasonable. In the MCMC procedure, for the initial values, the x–y coordinates of the center location of damage are uniformly sampled from
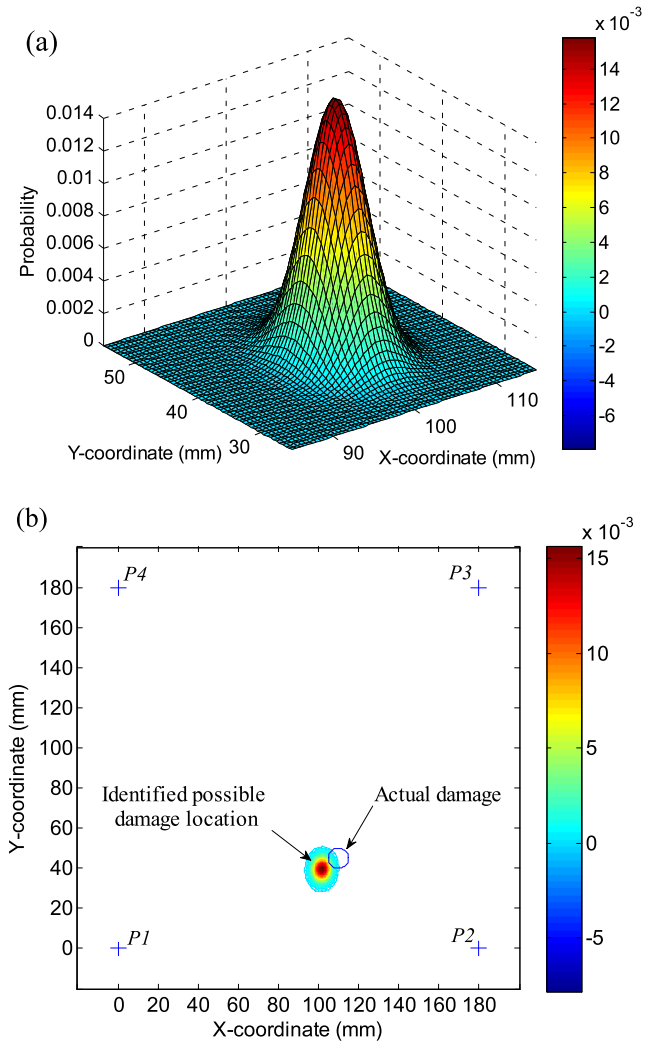
[0, 180] mm, and the wave velocity is uniformly sampled from [0, 3000] m s^{-1}. Figure 24(a) shows the samples of x–y coordinates of the center location of damage by MCMC, and figure 24(b) shows the simultaneously sampled wave velocity of the A_0 mode Lamb wave at 50 kHz. Again, for each parameter, a total of 100 000 samples are obtained and the first 40 000 are set as the 'burn-in' period. Figure 25 shows the histograms formed by the remaining 60 000 samples for each parameter. Figures 26(a) and (b) illustrate the fitted joint PDF of the x–y coordinates of the center location of damage in 3D and 2D views, respectively. The simulated damage is also labeled in figure 26(b) for comparison. The identified center location of damage is (101.6, 39.6) mm; the distance between the identified damage location and the actual center location is less than 9.99 mm with a relative error of 5.6% with respect to the sensor spacing (180 mm), again demonstrating the effectiveness of the proposed Bayesian localization approach.

7. Conclusions

This paper presents an investigation of the applicability of a Bayesian system identification theory for localizing damage in plate-like structures, while considering the uncertainties from modeling and measurement. After the ToF of scattered waves in each actuator–sensor path is measured by CWT, the Bayesian approach can adaptively identify the damage location and wave velocity. Rather than pinpointing the damage location in a single point by a traditional deterministic approach, the proposed Bayesian approach can provide a probabilistic description of the damage location and quantify the uncertainties of the identification results. Also, with wave velocity as an additional unknown, material properties of the plate-like structure could not be known *a priori*.

The effectiveness and applicability of the proposed Bayesian damage localization approach is validated by both numerical and experimental studies. The numerical study for an aluminum plate and the experimental study for a stiffened aluminum panel show that, for an isotropic plate-like structure, the Bayesian localization approach can not only identify the damage location quite accurately, but also estimate the wave velocity close to its actual value. The experimental study for a composite laminate demonstrates that, for an anisotropic plate-like structure, if the dependence of the wave velocity on the propagation direction is weak, it can assume the wave velocity is independent of the propagation direction and the proposed approach has the capability to localize the damage with error in a reasonable range.

Acknowledgments

References

[1] Farrar C R and Worden K 2007 An introduction of structural health monitoring *Phil. Trans. R. Soc.* A **315** 303–15
[2] Giurgiutiu V and Cuc 2005 A embedded NDE for structural health monitoring, damage detection, and failure prevention *Shock Vib. Dig.* **37** 83–105
[3] Su Z, Ye L and Lu Y 2006 Guided Lamb waves for identification of damage in composite structures: a review *J. Sound Vib.* **295** 753–80
[4] Raghavan A and Cesnic C S E 2007 Review of guided-wave structural health monitoring *Shock Vib. Dig.* **39** 91–114
[5] Raghavan A and Cesnic C E S 2007 Guided-wave signal processing using chirplet matching pursuits and mode correlation for structural health monitoring *Smart Mater. Struct.* **16** 355–66
[6] Kehlenbach M and Das S 2002 Identifying damage in plates by analyzing Lamb wave propagation characteristics *Proc. SPIE, Smart Nondestructive Evaluation for Health Monitoring of Structural and Biological System (Newport Beach, CA, 2002)* pp 364–75
[7] Tua P S, Quek S T and Wang Q 2004 Detection of cracks in plates using piezo-actuated Lamb waves *Smart Mater. Struct.* **13** 643–60
[8] Lemistre M and Balageas D L 2001 Structural health monitoring system based on diffracted Lamb wave analysis by multiresolution processing *Smart Mater. Struct.* **10** 504–11
[9] Su Z, Ye L and Bu X 2002 A damage identification technique for CF/EP composite laminates using distributed piezoelectric transducers *Compos. Struct.* **57** 465–71
[10] Lu Y, Ye L and Su Z 2006 Crack identification in aluminium plates using Lamb wave signals of a PZT sensor network *Smart Mater. Struct.* **15** 839–49
[11] Niethammer M, Jacobs L J, Qu J and Jarzynski J 2001 Time-frequency representations of Lamb waves *J. Acoust. Soc. Am.* **109** 1841–7
[12] Jeong H and Jang Y S 2000 Wavelet analysis of plate wave propagation in composite laminates *Compos. Struct.* **49** 443–50
[13] Niri E D and Salamone S 2012 A probabilistic framework for acoustic emission source localization in plate-like structures *Smart Mater. Struct.* **21** 035009
[14] Marzani A and Salamone S 2012 Numerical prediction and experimental verification of temperature effect on plate waves generated and received by piezoceramic sensors *Mech. Syst. Signal Process.* **30** 204–17
[15] Zhao X, Gao H, Zhang G, Ayhan B, Yan F, Kwan C and Rose J L 2007 Active health monitoring of an aircraft wing with embedded piezoelectric sensor/actuator network: I. Defect detection, localization and growth monitoring *Smart Mater. Struct.* **16** 1208–17
[16] Wang D, Ye L, Lu Y and Su Z 2009 Probability of the presence of damage estimated from an active sensor network in a composite panel of multiple stiffeners *Compos. Sci. Technol.* **69** 2054–63
[17] Wang D, Ye L and Lu Y 2009 A probabilistic diagnostic algorithm for identification of multiple notches using digital damage fingerprints (DDFs) *J. Intell. Mater. Syst. Struct.* **20** 1439–50
[18] Flynn E B, Todd M D, Wilcox P D, Drinkwater B W and Croxford A J 2011 Maximum-likelihood estimation of damage location in guided-wave structural health monitoring *Proc. R. Soc.* A **467** 2575–96
[19] Su Z, Wang X, Chen Z and Ye L 2009 On selection of data fusion schemes for structural damage evaluation *Struct. Health Monit.* **8** 223–41
[20] Zhou C, Su Z and Cheng L 2011 Probability-based diagnostic imaging using hybrid features extracted from ultrasonic Lamb wave signals *Smart Mater. Struct.* **20** 125005
[21] Yu L and Su Z 2012 Application of kernel density estimation in Lamb wave-based damage detection *Math. Probl. Eng.* **2012** 406521
[22] Beck J L and Katafygiotis L S 1998 Updating models and their uncertainties I: Bayesian statistical framework *ASCE J. Eng. Mech.* **124** 455–61
[23] Vanik M W, Beck J L and Au S K 2000 Bayesian probabilistic approach to structural health monitoring *ASCE J. Eng. Mech.* **126** 738–45
[24] Beck J L and Au S K 2002 Bayesian updating of structural models and reliability using Markov chain Monte Carlo simulation *ASCE J. Eng. Mech.* **128** 380–91
[25] Beck J L and Yuen K V 2004 Model selection using response measurements: Bayesian probabilistic approach *ASCE J. Eng. Mech.* **130** 192–203

[26] Jiang X and Mahadevan S 2008 Bayesian wavelet methodology for structural damage detection *Struct. Control Health Monit.* **15** 974–91

[27] Karandikar J M, Kim N H and Schmitz T L 2012 Prediction of remaining useful life for fatigue-damaged structures using Bayesian inference *Eng. Fract. Mech.* **96** 588–605

[28] Flynn E B and Todd M D 2010 A Bayesian approach to optimal sensor placement for structural health monitoring with application to active sensing *Mech. Syst. Signal Process.* **24** 891–903

[29] Haynes C and Todd M D 2012 Bayesian probabilistic modeling for damage assessment in a bolted frame *Proc. SPIE, Health Monitoring of Structural and Biological Systems (San Diego, CA, 2012)* p 83480D

[30] Yin T, Lam H F and Chow H M 2010 A Bayesian probabilistic approach for crack characterization in plate structures *Comput.—Aided Civ. Infrastruct. Eng.* **25** 375–86

[31] Ng C T, Veidt M and Lam H F 2009 Guided wave damage characterisation in beams utilising probabilistic optimisation *Eng. Struct.* **31** 2842–50

[32] Ciampa F and Meo M 2010 A new algorithm for acoustic emission localization and flexural group velocity determination in anisotropic structures *Composites* A **41** 1777–86

[33] Mallat S 1998 *A Wavelet Tour of Signal Processing* (London: Academic)

[34] Dunn W L and Shultis J K 2011 *Exploring Monte Carlo Methods* (Amsterdam: Elsevier)

[35] Nichols J M, Link W A, Murphy K D and Olson C C 2010 A Bayesian approach to identifying structural nonlinearity using free-decay response: application to damage detection in composites *J. Sound Vib.* **329** 2995–3007

[36] Stull C J, Nichols J M and Earls C J 2011 Stochastic inverse identification of geometric imperfections in shell structures *Comput. Methods Appl. Mech. Eng.* **200** 2256–67

[37] Diamanti K, Hodgkinson J M and Soutis C 2004 Detection of low-velocity impact damage in composite plates using Lamb waves *Struct. Health Monit.* **3** 33–41

[38] HKS Inc. 2005 *ABAQUS 6.5 Theory Manual*